Journal of Materials Chemistry C

ROYAL SOCIETY OF CHEMISTRY

PAPER

View Article Online
View Journal | View Issue

Cite this: J. Mater. Chem. C, 2020, 8, 3029

Tunneling-induced negative permittivity in Ni/MnO nanocomposites by a bio-gel derived strategy†

Peitao Xie,[a] Yifan Li,[b] Qing Hou,[c] Kunyan Sui,[a] Chunzhao Liu,*[a] Xueyan Fu,[b] Jiaoxia Zhang,[d] Vignesh Murugadoss,[ef] Jincheng Fan,[g] Yanpeng Wang,[h] Runhua Fan*[i] and Zhanhu Guo*[j]

One-dimensional wires are the most common building blocks in metamaterials. In this study, zero-dimensional nanoparticles connected by tunneling networks were used to construct metamaterials, thus providing a more flexible alternative for designing the geometrical configuration of metamaterials, particularly in nanodevices. The composites with nickel nanoparticles@MnO were prepared by a bio-gel derived strategy. Nickel nanoparticles were not connected geometrically, but the conductive network had been already formed, which was a tunneling-dominated percolative phenomenon demonstrated by the first-principles calculation. Negative permittivity was achieved in the composites, as the low-frequency plasmonic state could be generated in the tunneling nickel-networks. At the same time, negative susceptibility was observed due to the diamagnetism of the tunneling current loops. Electromagnetic simulations indicate that the composites have the potential for electromagnetic shielding (only 0.25 mm in thickness). It is believed that this study not only fills up the research gap in the influence of the tunneling effect on negative electromagnetic parameters but also opens up another way of preparing metamaterials by using zero-dimensional nanoparticles instead of one-dimensional wires.

Received 20th November 2019,
Accepted 3rd January 2020

DOI: 10.1039/c9tc06378a

rsc.li/materials-c

1. Introduction

Metamaterials with negative electromagnetic parameters have aroused a wave of research because of their fascinating properties and potential applications in the field of invisibility, imaging, antennae, sensors, wave funneling, dielectric enhancement, *etc.*[1–6] Metamaterials are typically composed of artificial periodic structure units, and their properties are fundamentally dependent on the geometrical shape of structure units rather than their component materials, thus indicating that metamaterials possess artificial properties.[7,8] Theoretical investigations indicated that negative electromagnetic parameters can also be attained in heterogeneous composites without clear periodic structures by virtue of the materials' intrinsic properties, as further demonstrated by many studies.[9–13] These materials are termed as random metamaterials or metacomposites with the advantage of truly practical applications owing to their large scale production, easy process and low cost.

It is worth noting that one-dimensional wires are the main building blocks in periodic or random metamaterials. Periodic metamaterials usually consist of metal wires and split-ring resonators (SRRs) when the metamaterials are applied in microwave devices, while other simplified shapes, such as double SRRs, U-shaped SRRs, cut wires, and fishnet topology, are designed to

[a] State Key Laboratory of Bio-fibers and Eco-textiles, Institute of Biochemical Engineering, College of Materials Science and Engineering, Qingdao University, Qingdao 266071, China. E-mail: czliu@qdu.edu.cn
[b] Key Laboratory for Liquid-Solid Structural Evolution and Processing of Materials (Ministry of Education), Shandong University, Jinan 250061, China
[c] Kathleen Lonsdale Materials Chemistry, Department of Chemistry, University College London, 20 Gordon Street, London WC1H 0AJ, UK
[d] School of Materials Science and Engineering, Jiangsu University of Science and Technology, Zhenjiang 212003, China
[e] Key Laboratory of Materials Processing and Mold (Zhengzhou University), Ministry of Education, National Engineering Research Center for Advanced Polymer Processing Technology, Zhengzhou University, Zhengzhou, China
[f] School of Materials Science and Engineering, North University of China, Taiyuan 030051, China
[g] College of Materials Science and Engineering, Changsha University of Science and Technology, Changsha 410114, China
[h] College of Chemistry and Chemical Engineering, Henan University, Kaifeng 475004, China
[i] College of Ocean Science and Engineering, Shanghai Maritime University, Shanghai 201306, China. E-mail: rhfan@shmtu.edu.cn
[j] Integrated Composites Laboratory (ICL), Department of Chemical and Biomolecular Engineering, University of Tennessee, Knoxville, Tennessee 37996, USA. E-mail: zguo10@utk.edu

† Electronic supplementary information (ESI) available. See DOI: 10.1039/c9tc06378a

optimize electromagnetic properties or match the wavelength at THz/optical frequency regions.[14–18] In the random metamaterials (*i.e.*, heterogeneous composites), negative electromagnetic parameters are obtained with the formation of conductive networks consisting of one-dimensional conductive paths.[19–25] These one-dimensional building blocks with large size can be easily fabricated by the conventional processing of materials, such as silk-screen printing and etching, but it is difficult to prepare metal wire arrays at nanoscale. In fact, replacing one-dimensional metallic wire arrays by zero-dimensional metal particle arrays as the building blocks of metamaterials will make the geometrical configuration of metamaterials more flexible, which is particularly helpful in nanodevices.[26]

The percolation phenomenon is a common behavior in random metamaterials; this can provide us with some inspiration to prepare metamaterials consisting of zero-dimension metallic nanoparticles.[27,28] In fact, the percolative mechanism is dominated by the tunneling effect rather than the observed "geometrical" conductive path.[29–31] In tunneling percolation, the conductive network is formed in the heterogeneous composites on increasing the content of metal fillers, though a geometrically-connected network is still absent.[32–37] This will provide a new design paradigm to replace the one-dimensional building blocks with zero-dimensional nanoparticles in metamaterials. Moreover, the question regarding whether the tunneling effect influences the negative permittivity in the random metamaterials is still unsolved.

Therefore, the objective of this study is to construct random metamaterials consisting of zero-dimensional metallic nanoparticles and to provide a better understanding of the influence of the tunneling effect on negative permittivity. The Ni/MnO nanocomposites have been constructed by a bio-gel inspired strategy; these composites inherit the nanostructures from their carbonate precursor during the topological transformation. The microstructure and composition were analyzed by field emission scanning electron microscopy (FESEM) and X-ray diffraction (XRD). The dielectric properties and permeability were tested in the frequency range from 5 MHz to 1 GHz. First-principles calculations were conducted based on the non-equilibrium Green's function and density functional theory, as implemented in the Atomistix ToolKit. The distance between nickel nanoparticles is controlled by the Ni/Mn ratio in the bio-gel precursor. With the increase in the nickel content, there are no geometrically connected nickel nanoparticles, but all nickel nanoparticles are in contact with each other electrically by tunneling. Meanwhile, the tunneling behavior is accompanied by the generation of negative permittivity, indicating that negative permittivity is attributed to "tunneling" rather than the "geometrical" network. Moreover, negative susceptibility was achieved due to the diamagnetic response of tunneling current loops under a high-frequency external magnetic field.

2. Experimental

2.1 Chemicals

Nickel chloride ($NiCl_2{\cdot}6H_2O$), manganous chloride ($MnCl_2{\cdot}4H_2O$) and ammonium hydrogen carbonate (NH_4HCO_3) were purchased from Sinopharm Chemical Reagent Co., Ltd, China. The agar was purchased from Aladdin Reagent Co., Ltd. The chemicals were obtained as chemically pure grade products, and used without any further treatment. The purity of hydrogen (H_2) was 99.9%.

2.2 Biomimetic preparation of $NiCO_3/MnCO_3$ precursors

Precursor solutions were prepared by the addition of 12 g agar powders into a 200 mL aqueous solution containing x mol $NiCl_2{\cdot}6H_2O$ and y mol $MnCl_2{\cdot}4H_2O$ ($x + y = 0.08$) with heating at 100 °C for 20 min. Precursor solutions were cooled down and solidified at 25 °C for 2 h and then, 200 mL 1.2 mol L^{-1} NH_4HCO_3 aqueous solution was poured onto the solidified precursor gel. The nanoparticles of $NiCO_3$ and $MnCO_3$ were formed with the infiltration of NH_4HCO_3 into the gel for 48 h at 25 °C. The precursor powders were obtained after dissolving the agar gel in deionized water at 100 °C and drying at 60 °C. The nickel content in the nanocomposite particles was controlled by the ratio of Ni/Mn; in this paper, the ratios of 20 : 80, 40 : 60 and 60 : 40 were used, and the corresponding composites were denoted as Ni20, Ni40 and Ni60.

2.3 The preparation of Ni/MnO nanoparticles and bulk nanocomposites

The Ni/MnO nanoparticles were produced by heating precursor powders at 600 °C for 6 h in an Ar atmosphere containing 3% H_2. Afterwards, the Ni/MnO bulk composites were prepared by dry pressing at 30 MPa and then sintered at 1050 °C for 1 h in H_2 atmosphere.

2.4 Models and computational methods

The tunneling currents were studied using the first-principles method based on the non-equilibrium Green's function (NEGF) and density functional theory (DFT), as implemented in the Atomistix ToolKit (ATK). The model consists of three parts, namely, two nickel electrodes and the vacuum gap between them. We model the system with two 3×3 Ni(100), Ni(110) and Ni(111) electrodes, respectively.

2.5 Characterization and measurement

The microstructure of the composites was studied using a field emission scanning electron microscope (FESEM, Hitachi SU-70, Tokyo, Japan). The phase identifications of the composites were investigated at room temperature by X-ray diffraction (XRD; Tokyo, Japan) using the Rigaku D/max-rB X-ray with Cu Kα radiation. The size of the particles was measured from SEM images using a Nano Measurer software. The dielectric parameters, including ac conductivity, reactance as well as complex permittivity of the composites, were measured by Agilent E4991 Precision Impedance Analyzer with a 16453A dielectric test fixture. After calibration and compensation for the analyzer, the samples were placed between the two planar electrodes, and impedance data were obtained, which could be converted to permittivity and ac conductivity data by calculations.[12,36] The test fixture of 16454A was used to measure the complex permeability, μ, under an ac current of 2 mA, using the Agilent E4991 Precision Impedance Analyzer. The theory for permeability measurements

is the one-turn coil method. The toroidal samples were prepared with the dimensions of 7 × 20 × 2 mm.[37]

3. Results and discussion

The preparation process is illustrated in Fig. 1. After the Ni^{2+} solution was solidified as a gel by agar, the composites consisting of $NiCO_3$ and $MnCO_3$ formed with the gradual infiltration of HCO_3^-. After the treatment in H_2 atmosphere at 600 °C, the $NiCO_3/MnCO_3$ precursor reduced to Ni/MnO composites, where nickel nanoparticles contact with each other. After being sintered at 900 °C, these nickel nanoparticles started to separate from each other, but they were still electrically connected by the tunneling current, as tiny nanoparticles grew into bigger ones.

3.1 Microstructure and phase characterization

Fig. 2a shows the XRD patterns of the as-prepared $NiCO_3/MnCO_3$ precursors with different nickel content. It is observed that all the diffraction peaks of as-prepared $NiCO_3/MnCO_3$ precursors correspond to the rhodochrosite phase of $MnCO_3$ (standard JCPDS no. 44-1472), which has a hexagonal space group of $R\bar{3}c$ (no. 167) and lattice parameters of $a = b = 4.7901$ Å, and $c = 15.694$ Å. There is no visible $NiCO_3$ phase peak detected in its XRD pattern, because its diffraction intensity is not strong enough compared with that of $MnCO_3$.[38–40] The peak intensity weakens with the increase in nickel content, also indicating the low crystallization grade of $NiCO_3$. After reduction reaction at 600 °C, the XRD patterns of Ni/MnO (in Fig. 2b) show that the powder consists of nickel (JCPDS card #04-0850) and manganosite (MnO) (JCPDS card #07-0230) without other phases, which indicates that $NiCO_3$ is completely decomposed and reduced to nickel. In other words, the Ni/MnO composites powders were successfully prepared by biomimetic process and *in situ* reduction.[38]

Fig. 3 depicts the SEM images of $NiCO_3/MnCO_3$ precursor particles with different nickel content. The precursor particles with Ni/Mn = 0 : 100 show cube-like shape with ~12 μm size (in Fig. 3a). The morphology gradually changes into olivary shape when Ni/Mn = 40 : 60 (in Fig. 3c and e), while the particles show spherical morphology when Ni/Mn = 60 : 40 (in Fig. 3g). At high magnification, it can be seen that the precursor particles consist of many nanoparticles (Fig. 3b, d, f and h), and their size decreases with the increase in nickel content (about 400 nm when Ni/Mn = 0 : 100, 70 nm when Ni/Mn = 20 : 80, 45 nm when Ni/Mn = 40 : 60 and 30 nm when Ni/Mn = 60 : 40). Hence, the addition of nickel can accelerate the nucleation process of precursors, and further influence their morphologies.[38,40]

Fig. 4 shows the SEM images of the Ni/MnO powder with different nickel content. Compared with Fig. 3, the morphology of the precursor particles was maintained after the reduction process. At high magnification, the tiny nickel nanoparticles are on the walls of the MnO framework. The MnO framework is porous due to the decomposition of carbonate. The nickel particles are ~20 nm in size and uniformly dispersed on the wall of the MnO framework when Ni/Mn = 20 : 80 (in Fig. 4b), while the nickel particles have size of ~30 nm when Ni/Mn = 40 : 60 (in Fig. 4d). The distance between nickel nanoparticles decreases with increasing nickel content, but they are still isolated on the MnO matrix. Further increasing the nickel content leads to the interconnection of nickel particles when Ni/Mn = 60 : 40 (in Fig. 4f). Therefore, Ni/MnO nanoparticles can be obtained, which inherit the nanostructure of the carbonate precursor. Thus, the bio-gel strategy provides a method for the preparation of metal–ceramic nanocomposites.[40,41]

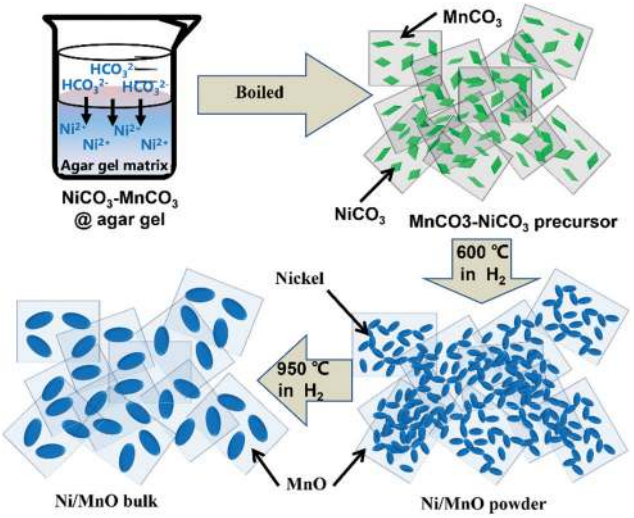

Fig. 1 Illustration of the preparation of Ni/MnO composites *via* a bio-gel-derived strategy.

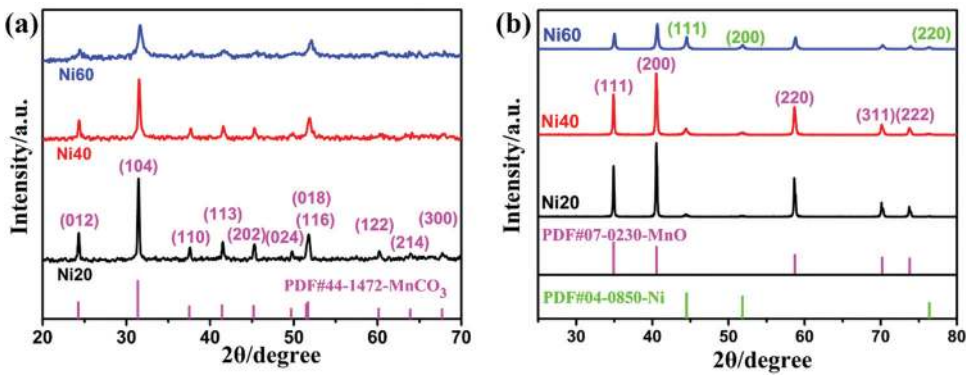

Fig. 2 XRD patterns of (a) $NiCO_3/MnCO_3$ precursors and (b) Ni/MnO nanoparticles with different nickel content.

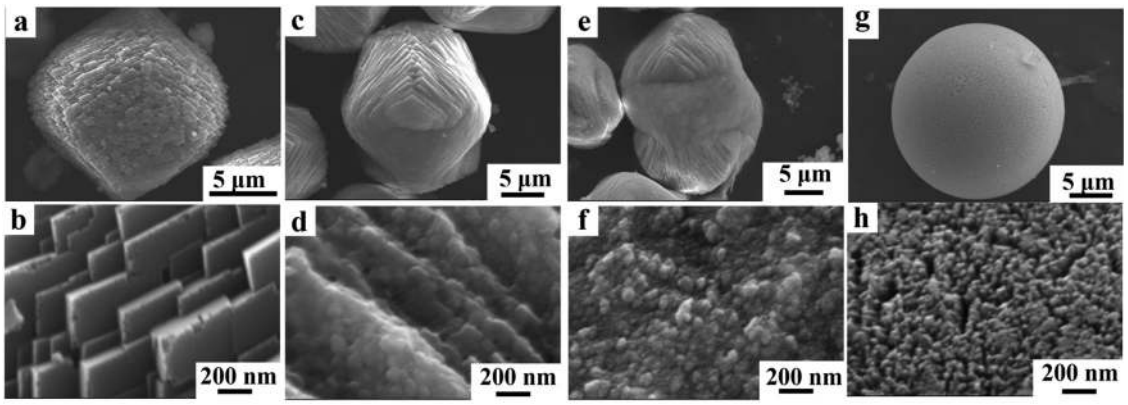

Fig. 3 SEM images of $NiCO_3/MnCO_3$ precursor particles with different Ni/Mn ratios. (a and b) 0 : 100; (c and d) 20 : 80; (e and f) 40 : 60; (g and h) 60 : 40.

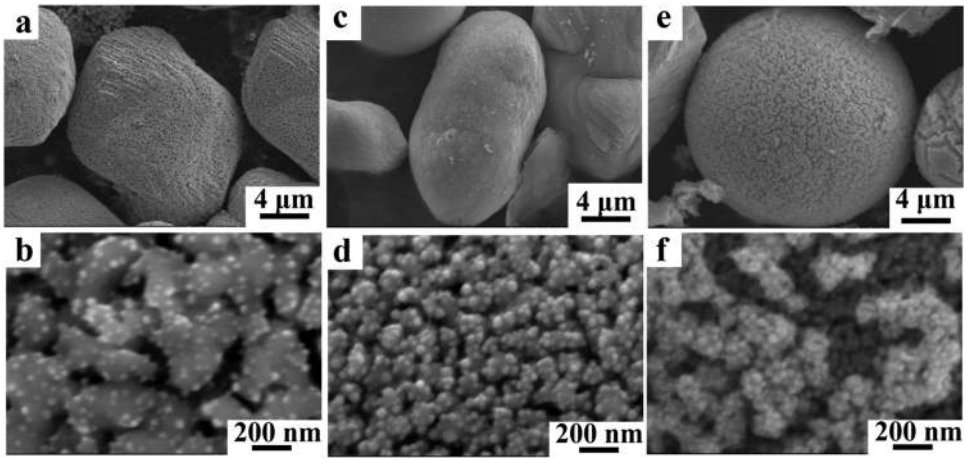

Fig. 4 SEM images of Ni/MnO powder with different Ni/Mn ratios. (a and b) 20 : 80; (c and d) 40 : 60; (e and f) 60 : 40.

The fracture surface morphology of Ni/MnO bulk nanocomposites with different nickel content are shown in Fig. 5. In Fig. 5a and b, the nickel nanoparticles were isolated and uniformly distributed in the Ni20 composite. The grain size of MnO is ~400 nm after the sintering process. The nickel nanoparticles are ~102 nm in size with evident growth compared with the Ni/MnO powder (Fig. 4b) (the size distribution in Fig. S1, ESI†), but the distance among nickel nanoparticles increases to

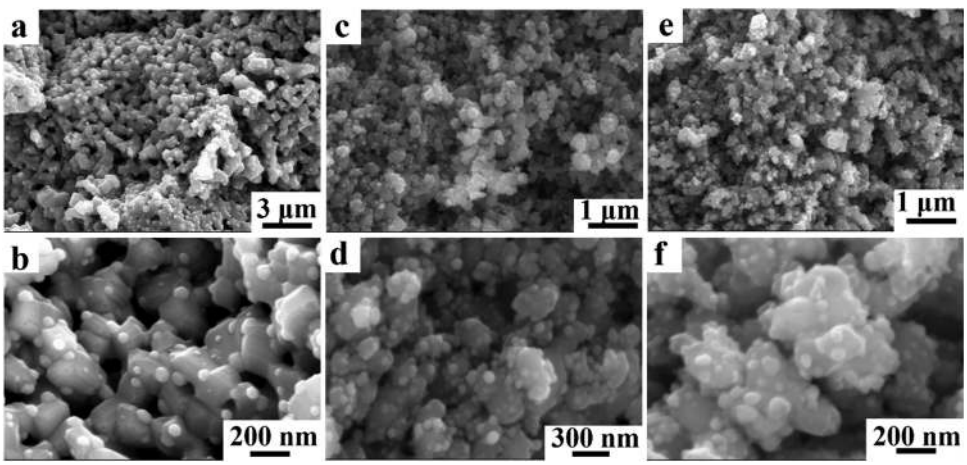

Fig. 5 SEM images of Ni/MnO bulk nanocomposites with different nickel content. (a and b) Ni20; (c and d) Ni40; (e and f) Ni60.

~100 nm. In the Ni40 composite, the nickel particle size is ~59 nm (the size distribution in Fig. S2, ESI†) and the distance among nickel particles is ~50 nm (in Fig. 5c and d). Moreover, the mean size of the nickel particles is ~53 nm in the Ni60 composite (the size distribution in Fig. S3, ESI†), while the mean distance among nickel particles is only ~20 nm (in Fig. 5e and f). It is worth noting that nickel nanoparticles were isolated and uniformly distributed in the Ni60 composite, while these nickel nanoparticles connected with each other in the composite powder (in Fig. 4f), which is attributed to the growth of nickel nanoparticles during the sintering process. Therefore, the metal–ceramic composites without geometrical conductive networks have been successfully obtained, and can be used to study the tunneling-induced negative permittivity behavior.[27,28] In fact, the following discussion of electrical conductivity indicated that the nickel conductive network has been formed in Ni60 composites because of the tunneling effect among nearest-neighbor nickel nanoparticles though nickel nanoparticles were isolated geometrically, while nickel nanoparticles were isolated not only geometrically but also electrically in other samples. The alternating current (ac) conductivity was investigated and discussed in the following section.

3.2 Alternating current conductivity of the Ni/MnO bulk nanocomposites

The frequency dependence of ac conductivity (σ_{ac}) of Ni/MnO bulk nanocomposites with different nickel content is shown in Fig. 6a. σ_{ac} increases with the increase in the frequency for MnO bulk, Ni20 and Ni40, while σ_{ac} decreases with the increase in the frequency for Ni60. The different frequency dispersion of ac conductivity indicates different conductive mechanisms and a percolating phenomenon, which can be described by percolation theory.[36] In the typical percolation theory, metallic particles are isolated below the percolation threshold, so hopping conductivity is usually dominant, following the power law $\sigma_{ac} \propto \omega^n$ $(0 < n < 1)$, where ω is the angular frequency of external electrical field and n is the exponential parameter.[42,43] The calculation results using power law are given as solid lines in Fig. 6a and Table S1 (ESI†), agreeing well with the experimental data, which suggests a hopping conductive behavior. In contrast, σ_{ac} shows a metal-like behavior in Ni60, as its conductivity decreases with the increase in frequency due to the high-frequency skin effect. The skin effect is described by skin depth: $\delta = (2/\omega\sigma_{dc}\mu)^{0.5}$, where δ is the skin depth, σ_{dc} is the dc conductivity, and μ is the static permeability.[44] The skin depth gradually decreases with the increase in frequency, leading to the decrease in conductivity because of the reduction in the effective conductive sectional area.

It is worth noting that the nickel nanoparticles of Ni60 are still isolated in geometry and uniformly distributed in the composites, though the distance among these nickel particles is very small (in Fig. 5f). Therefore, this metal-like conductivity is attributed to the tunneling current occurring among nickel nanoparticles. It is well known that there are two conductivity mechanisms in the heterogeneous composites consisting of metal particles and insulative matrix: percolation in a continuous geometrical network and in a tunneling network.[45,46] The tunneling current could be formed when the distance between two isolated conductive particles is small enough. For example, the tunneling distance in carbon black/polymer composites is a few nanometers, while the tunneling distance (~15 nm) is much larger in the composites with wolfram particles dispersed in Al_2O_3 matrix because of the metal's better conductivity.[47–50] Theoretically, the tunneling current is dependent on the intrinsic property of conductive particles, matrix materials and the distance between two conductive particles. In this study, the potential barrier of tunneling current is lower, as the nickel nanoparticles grow on the walls of the MnO matrix rather than being embedded in MnO, and the actual potential barrier comes from the air between nickel particles rather than from insulating MnO.[51] Besides, nickel has good electrical conductivity. Therefore, it is easier to generate tunneling current in the Ni/MnO composites. The schematic of the tunneling network is shown in Fig. 6b. The nickel nanoparticles have an effective tunneling distance according to tunneling theory, so it is only the contribution of nearest-neighbor tunneling that really counts.[47] The global electrical connectivity across the whole composite is dominated by the nearest-neighbor tunneling rather than the "geometrical" network or the particles far away from each other.[49]

To further investigate the influence of the tunneling effect on the conductivity of Ni/MnO composites, first-principles

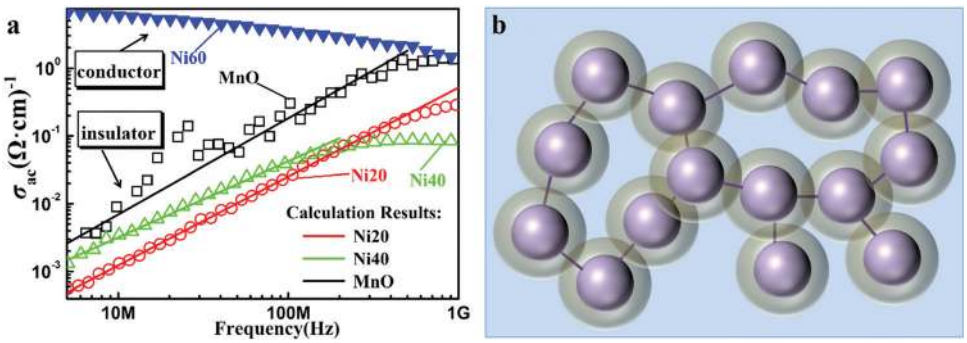

Fig. 6 (a) Frequency dependences of ac conductivity for Ni/MnO bulk nanocomposites with different nickel content. (b) The schematic of a conductive network formed by tunneling current. The solid circles in (b) represent the nickel nanoparticles, while the gray shells represent the effective tunneling distance, and the solid lines represent the tunneling currents occurring among nearest-neighbor nickel nanoparticles.

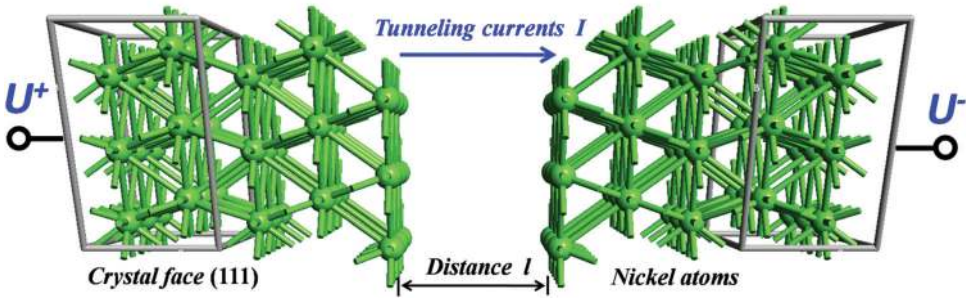

Fig. 7 Models of the (111) crystal face to calculate tunneling conductivity using first-principles method.

Table 1 Parameters and results of calculations using the first-principles method

Crystal face	Distance l (nm)	Voltage U (V)	Current I (μA)	σ (S cm^{-1})
(111)	0.5	1	30	5.7156×10^3
(110)	0.5	1	27	5.1440×10^3
(100)	0.5	1	29	5.5251×10^3

calculations were conducted based on non-equilibrium Green's function and density functional theory, as implemented in the ATK software package.[52] The models are shown in Fig. 7, Fig. S4 and S5 (ESI†), and calculation parameters and results are shown in Table 1. It can be observed that the tunneling conductivity is rarely influenced by the different crystal face of nickel. The calculated conductivity is about 5.5×10^3 S cm^{-1}, which is much smaller than that of bulk nickel ($\sim 10^5$ S cm^{-1}); this is due to the high tunneling resistance.[13,53] These calculated results represent the conductivity between two nickel particles rather than that of the actual composites, which leads to the deviation from experimental results, because the conductivity of the nanocomposites is heavily influenced by the number of nearest-neighbor tunneling particles and their effective conduction area. First, the total area of nickel nanoparticles in Ni60 nanocomposites was estimated by a Nano Measurer software (in Fig. S3, ESI†), only covering 5.84% of total area of SEM images. Besides, the number of nickel particles that can form a tunneling-dominated conductive loop is much smaller than that seen in Fig. 5f, because only the nearest-neighbor tunneling can contribute to the effective conductivity of the nanocomposites. As a result, the actual conductivity is lower than the calculated value by ~ 3 orders of magnitude, suggesting that the calculated results are right and reasonable. As the tunneling effect has been obtained in Ni/MnO composites, the tunneling-induced negative permittivity is investigated in the next section.

3.3 Permittivity spectra of the Ni/MnO bulk nanocomposites

Frequency dependence of real permittivity (ε') for Ni/MnO composites with different nickel contents is shown in Fig. 8. ε' is positive for the composites with low nickel content and significantly increases with the increase in the nickel content due to the enhanced interfacial polarization (Fig. 7a).[27,28] The polarization across the nickel nanoparticle/MnO interface indicates that any pair of adjacent nickel particles separated by an insulative gap can be regarded as a microcapacitor; accordingly, the composite consists of thousands of microcapacitors and thus has huge permittivity (in the inset of Fig. 8a).[54] This so-called Maxwell–Wagner–Sillars effect, coming from the interfacial polarization, leads to the dielectric enhancement in many conductor–insulator composites.[12,55] In other words, the nickel electrons were localized in the isolated nickel nanoparticles and polarized under external alternating electrical field, thus acting as an electric dipole; hence, these samples had positive permittivity. Positive permittivity shows capacitive character, which is demonstrated by equivalent circuit analysis (in Fig. S6a, ESI†), which was performed using the

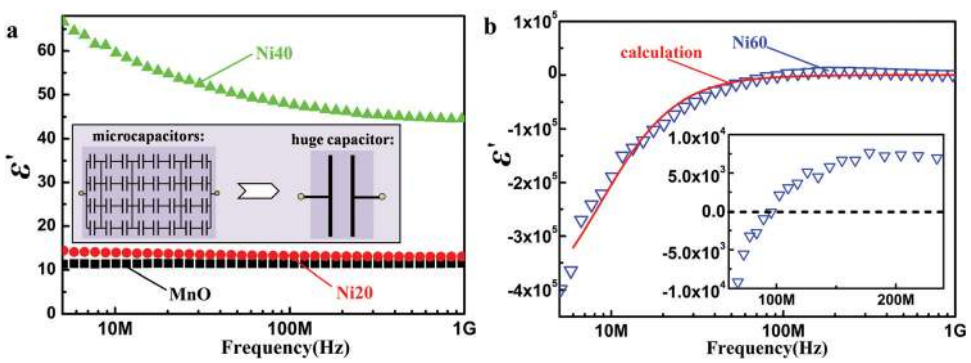

Fig. 8 Frequency dependence of real permittivity (ε') for Ni/MnO nanocomposites with different nickel content. The inset in (a) is the schematic of permittivity enhancement with the increase in nickel content. The solid line in (b) is the calculation result using the Drude model, indicating plasma-like negative permittivity.

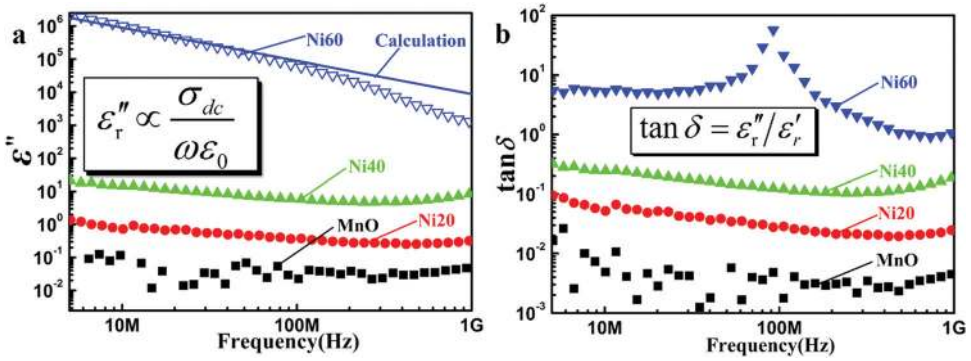

Fig. 9 Frequency dependence of (a) imaginary permittivity (ε'') and (b) dielectric loss tangent ($\tan\delta$) for Ni/MnO nanocomposites with different nickel content. The solid lines in (a) are the calculation results using $\varepsilon'' \propto \sigma_{dc}/\omega\varepsilon_0$, indicating conduction loss.

ZSimpwin software. The optimal equivalent circuit was chosen with the smallest chi square value (about 10^{-5}) and the error in the value of the circuit element is less than 5%. Besides, the real permittivity of MnO and Ni20 remains steady over the 5–1000 MHz frequency range, and their dielectric loss is extremely low ($\tan\delta \approx 0.05$ in Fig. 9b), so they have the potential as broadband dielectric materials, such as dielectric materials in capacitors, circuit boards and microwave dielectric materials.[28]

On further increasing the nickel content, negative permittivity is achieved in the Ni60 composite. Theoretically, negative permittivity is derived from the damped motion of free electrons rather than directly from energy storage, so negative permittivity behavior does not violate the law of conservation of energy. Similar results were found in other heterogeneous composites; negative permittivity is considered to be attributed to the plasma oscillation of free electrons in conductive network.[10–13,56] According to the discussion above, there is no "geometrical" conductive network existing in the Ni60 composites (in Fig. 5f). This indicates the tunneling-induced negative permittivity since the plasma oscillation of free electrons can only occur in the tunneling nickel network. In the Ni60 composite, the free electrons could move in the tunneling conductive network, and performed simple harmonic motion under external altering electrical field, that is, plasma oscillation; thus, the negative permittivity could be achieved. The simple harmonic motion in the conductive nickel network indicated inductive character; therefore, the imaginary part of impedance (inductance) was positive (in Fig. S6, ESI†). In previous investigations, the particle size of the conductive phase was much larger than the effective tunneling distance, or a geometrical conductive network has been clearly formed and observed, leading to the fact that the influence of tunneling effect on negative permittivity was completely neglected.[11–13,16–19] The tunneling-induced negative permittivity can also be explained well by the Drude model:[13]

$$\varepsilon_r' = 1 - \frac{\omega_p^2}{\omega^2 + \omega_\tau^2} \quad (1)$$

$$\omega_p = \sqrt{\frac{n_{eff}e^2}{m_{eff}\varepsilon_0}} \quad (2)$$

where ε_0 is vacuum permittivity (8.85×10^{-12} F m^{-1}), ω_τ is the damping constant, $\omega_p = 2\pi f_p$ is the plasmon angular frequency, n_{eff} is the effective concentration of the electron, ω is the angular frequency of the external electric field, and m_{eff} is the effective weight of the electron. The solid line in Fig. 8b is the calculation result using the Drude model *via* an iterative method in OriginPro 8.5 software, agreeing well with the experimental data with a high reliability factor $R^2 = 0.98622$. The plasmon frequency, f_p, is only 5.99 GHz, which is much smaller than that of bulk nickel (1.58×10^6 GHz), because the low-dimensional nickel structure and porous MnO framework can both lead to a dilution of the effective concentration of electrons (a decrease of n_{eff}).[57,58] It is concluded that the tunneling effect is also the mechanism for negative permittivity, as the long-distance movement of free electrons is the sufficient condition for the plasma oscillation of free electrons.[19–25] Interestingly, the experimental and theoretical data of negative permittivity in Ni/MnO composites are similar to those of other heterogeneous composites in the previous investigations,[11–13,16–19] indicating that zero-dimensional metallic nanoparticles connected by the tunneling effect can replace the one-dimensional metallic wires to construct metamaterials with negative electromagnetic parameters.

Fig. 9 depicts the frequency dependence of imaginary permittivity (ε'') and dielectric loss tangent ($\tan\delta$) for Ni/MnO composites with different nickel content. It is observed that ε'' increases with increasing nickel content (in Fig. 9a). Dielectric loss consists of conduction loss and polarization loss. The ε'' of MnO, Ni20 and Ni40 are almost constant in the 5–1000 MHz region, indicating that polarization loss is the main loss mechanism. On further increasing the nickel content, ε'' of Ni60 has a linear relationship with frequency in the log–log plot in Fig. 9a, which could be well explained by the conduction loss as follows:[11,12]

$$\varepsilon'' = \frac{\sigma_{dc}}{\omega\varepsilon_0} \quad (3)$$

where σ_{dc} is the direct current conductivity. The solid line in Fig. 9a is the calculation result using eqn (3), well fitted with experimental data in the 5–100 MHz region, which indicates that conduction loss is dominant. However, the calculation results clearly start to deviate from experimental data at the higher frequency region (above 100 MHz), because some tunneling-related nickel

nanoparticles turn into polarization responses at higher frequency.[11] A loss peak is observed in the Ni60 composite, corresponding to the negative–positive switching point of negative permittivity.[36,37] Interestingly, the tunneling-dominated tan δ is smaller than most other negative-permittivity composites consisting of metals and ceramics, which can be attributed to high tunneling resistance and low leakage current (in Table 1).[28,47,49] Therefore, we can conclude that tunneling is another mechanism for the generation of negative permittivity. Tunneling-induced negative permittivity will have great significance on improving the design methods of metamaterials, because we will no longer need to introduce metallic wires and split-rings into metamaterials; instead, metallic particle arrays will be used to construct metamaterials. This will endow the geometrical configuration of metamaterials with more freedom, which is particularly helpful for designing nanodevices.

3.4 Permeability spectra of the Ni/MnO bulk nanocomposites

Fig. 10a depicts the frequency dependence of real permeability (μ') for Ni/MnO composites with different nickel content. The real permeability (μ') of MnO almost remains at 1 due to its non-magnetism, and the μ' of Ni20 and Ni40 increases with the increase in nickel content. However, the μ' of Ni60 is smaller than 1, suggesting negative susceptibility, and its value decreases with the increase in frequency.[13,36] In fact, the conductive network has already been formed in Ni60 due to tunneling current, and once it is put under a high-frequency magnetic field, there would be hundreds of induced micro current loops inside the tunneling network.[13,19,25,44] The induced magnetic field from current loops would be opposite to the external magnetic field (illustrated in the inset of Fig. 10a), leading to negative susceptibility.[59] In other words, negative susceptibility is attributed to the diamagnetic response of the tunneling network, which makes Ni/MnO composites promising candidates for novel magnetic materials. Fig. 10b depicts the frequency dependence of imaginary permeability (μ''). μ'' is small when the nickel content is low, and significantly increases with the increase in the nickel content, but decreases with the increase in frequency (in Fig. 10b). It is well known that magnetic loss mainly originates from hysteresis loss, eddy current effects and magnetic resonance at the radio-frequency region.[60] While hysteresis loss can be negligible in the weak field, eddy current loss can be expressed as follows:[61]

$$\mu'' = 2\pi\mu_0(\mu'^2)\sigma_{dc}D^2f/3 \quad (4)$$

where D is the effective diameter of metal particles. If the magnetic loss simply derives from the eddy current loss, the value of $\mu''/(\mu'^2 f)$ should be nearly constant across the test frequency range. As can be seen from the inset of Fig. 10b, the values at different frequencies are close to each other ($\approx$7) over the 500–1000 MHz region and quite different from each other over the 5–500 MHz region. Hence, eddy current loss dominates the magnetic loss over the 500–1000 MHz region, while eddy current loss does not dominate the magnetic loss over the 5–500 MHz region. This further demonstrates the contribution of tunneling networks to negative susceptibility.

3.5 Electromagnetic simulation and shielding effectiveness

To investigate the interaction between electromagnetic waves and the Ni60 composite, the electromagnetic propagation properties were further investigated by numerical simulations using the Computer Simulation Technology software. The detailed simulation process is presented in the supporting information. Shielding effectiveness (SE) is the main evaluation criterion of suppressing electromagnetic interference (EMI). SE total (SE_T) includes SE absorption (SE_A), and SE reflection (SE_R).[62] The simulated SE_T results of Ni60 are shown in Fig. 11a. The SE_T value increased with the increase in the thickness of the composite, whereas it decreased with the increase in the frequency in the 10–1000 MHz region. Besides, the SE_T value of Ni60 composites could reach the target level of 20 dB for commercial applications at the 10–1000 MHz region with the thickness of shielding layer being 0.5 mm. The thickness of the shielding layer can even be as low as 0.25 mm at the 10–400 MHz region, and SE_A and SE_R are also high enough (in Fig. S8, ESI†). The conductive nickel network is formed due to the tunneling effect among the nickel nanoparticles, which leads to the high SE_R, because the effective thickness of the nickel network is more than the skin depth of metal nickel ($\sim$0.011 mm at 100 MHz). Furthermore, epsilon-negative materials have high dielectric loss and the incident

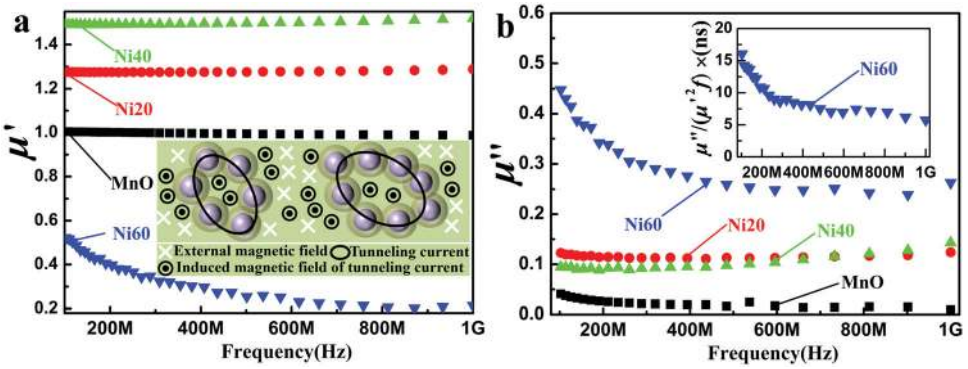

Fig. 10 Frequency dependence of (a) real permeability (μ') and (b) imaginary permeability (μ'') for Ni/MnO nanocomposites with different nickel content. The inset in (a) is the schematic of negative susceptibility ($\mu' < 1$) due to the induced magnetic field of tunneling current.

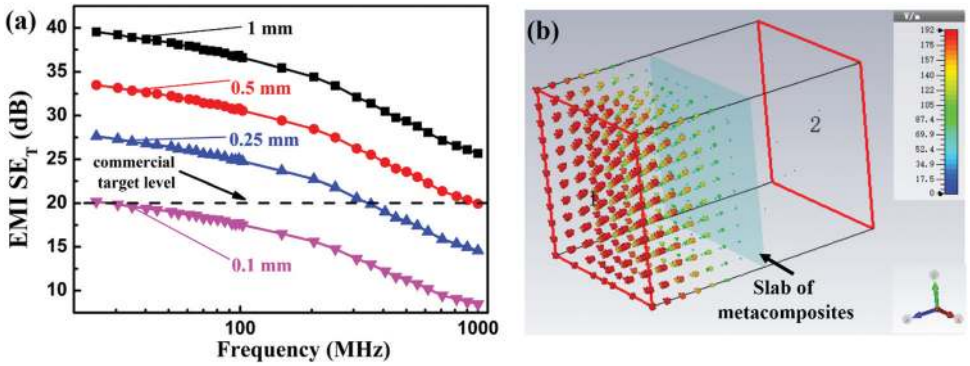

Fig. 11 (a) Frequency dispersion of EMI SE_T of Ni60 metacomposites with different thickness. (b) The distribution of the electric field vector of Ni60 metacomposites at 501.19 MHz with 0.5 mm thickness.

electromagnetic wave can be completely absorbed, leading to high SE_A. The negative permittivity coming from the tunneling nickel network in the Ni60 composite contributes to the high SE value and excellent electromagnetic shielding property. The excellent electromagnetic shielding property is further demonstrated by the distribution of the electric field vector in Fig. 11b. As we can see from Fig. 11b, there no electric field vectors exist at the other side of the composites, indicating that the Ni60 composites successfully suppress the electromagnetic interference. Therefore, we can conclude that excellent shielding effectiveness, with the advantage of thin layers, makes Ni/MnO composites highly competitive to conventional metals and carbon shielding materials.[63] In fact, electromagnetic shielding is relatively difficult at the lower frequency band, so this study is significant in demonstrating that epsilon-negative materials can contribute excellent electromagnetic shielding property at the MHz frequency region. Besides, such electromagnetic shielding at the MHz frequency region can contribute to high-end capacitors with the advantage of high frequency and high capacity by stacking epsilon-negative materials with epsilon-positive materials.[6] These materials can also be used as no-wire-wound inductors with higher quality factor and simple geometrical configuration.[13] Finally, these epsilon-negative composites also have potential applications in microwave attenuation materials, as the composites have high dielectric loss.[12]

4. Conclusion

In conclusion, Ni/MnO nanocomposites were prepared by a bio-gel-inspired strategy and *in situ* reduction transformation. The distance between nickel nanoparticles is controlled by the Ni/Mn ratio in the bio-gel precursor and the reduction process. Although nickel nanoparticles are still isolated and not connected by a geometrical network, an electrical percolating behavior appears, accompanied by a change in the conductive mechanism from hopping conduction to metal-like conduction. In other words, a tunneling phenomenon is observed, which is further demonstrated by first-principles calculations. Meanwhile, the plasma-like negative permittivity is achieved along with tunneling behavior and well explained by the Drude model. The dielectric loss is dominated by conduction loss coming from the tunneling network. Moreover, negative susceptibility is obtained and attributed to the diamagnetic response of tunneling current loops. It is believed that this study could not only provide guidance for revealing the mechanism of negative permittivity but also provide a new design paradigm for negative electromagnetic parameter materials. The Ni/MnO nanocomposites can be regarded as promising candidates for random metamaterials, promoting the applications of negative permittivity metamaterials.

Conflicts of interest

There are no conflicts to declare.

Acknowledgements

The authors are grateful for helpful suggestions from Lingyuan Kong and Shuai Zhang (Institute of Physics, Chinese of Academy of Sciences). The authors thank Yulin Wu for her helping on first-principles calculation. This study was supported by the National Natural Science Foundation of China [grant no. 51871146, 51803119, 51771108], Innovation Program of Shanghai Municipal Education Commission, and Key Research and Development Project of Shandong Province [grant no. 2019GSF109079].

References

1 (*a*) R. Shelby, D. Smith and S. Schultz, *Science*, 2001, **292**, 77–79; (*b*) T. Ergin, N. Stenger, P. Brenner, J. Pendry and M. Wegener, *Science*, 2010, **328**, 337–339; (*c*) H. Wu, X. Huang and L. Qian, *Eng. Sci.*, 2018, **2**, 17–25; (*d*) J. C. Xu, Y. A. Hao, K. Bi, R. Zhang, S. G. Huang and J. Zhou, *Eng. Sci.*, 2019, **6**, 30–35.
2 J. Hunt, T. Driscoll, A. Mrozack, G. Lipworth, M. Reynolds, D. Brady and D. Smith, *Science*, 2013, **339**, 310–313.
3 (*a*) Z. Wang, X. Fu, Z. Zhang, Y. Jiang, M. Waqar, P. Xie, K. Bi, Y. Liu, X. Yin and R. Fan, *J. Cleaner Prod.*, 2019, **234**, 588–596; (*b*) X. Zhu, J. Yang, D. Dastan, H. Garmestani, R. Fan and Z. Shi, *Composites, Part A*, 2019, **125**, 105521; (*c*) K. Sun, P. Xie, Z. Wang, T. Su, Q. Shao, J. Ryu, X. Zhang, J. Guo, A. Shankar, J. Li, R. Fan, D. Cao and Z. Guo, *Polymer*, 2017, **125**, 50–57.

4 (*a*) H. Gu, X. Xu, M. Dong, P. Xie, Q. Shao, R. Fan, C. Liu, S. Wu, R. Wei and Z. Guo, *Carbon*, 2019, **147**, 550–558; (*b*) K. Sun, J. Xin, Z. Wang, S. Feng, Z. Wang, R. Fan, H. Liu and Z. Guo, *J. Mater. Sci.*, 2019, **30**, 14745–14754; (*c*) K. Sun, J. Dong, Z. Wang, Z. Wang, G. Fan, Q. Hou, L. An, M. Dong, R. Fan and Z. Guo, *J. Phys. Chem. C*, 2019, **123**, 23635–23642.
5 K. Sun, R. Fan, X. Zhang, Z. Zhang, Z. Shi, N. Wang, P. Xie, Z. Wang, G. Fan, H. Liu, C. Liu, T. Li, C. Yan and Z. Guo, *J. Mater. Chem. C*, 2018, **6**, 2925–2943.
6 Z. Shi, J. Wang, F. Mao, C. Yang, C. Zhang and R. Fan, *J. Mater. Chem. A*, 2017, **5**(28), 14575–14582.
7 C. Soukoulis, S. Linden and M. Wegener, *Science*, 2007, **315**, 47–49.
8 W. Padilla, D. Basov and D. Smith, *Mater. Today*, 2006, **9**(7), 28–35.
9 S. Chui and L. Hu, *Phys. Rev. B: Condens. Matter Mater. Phys.*, 2002, **65**(14), 144407.
10 (*a*) X. Huang, R. Yin, L. Qian, W. Zhao, H. Liu, C. Liu, J. Fan, H. Hou, J. Zhang and Z. Guo, *Ceram. Int.*, 2019, **45**, 17784–17792; (*b*) C. Cheng, R. Fan, Z. Wang, Q. Shao, X. Guo, P. Xie, Y. Yin, Y. Zhang, L. An, Y. Lei, J. Ryu, A. Shankar and Z. Guo, *Carbon*, 2017, **125**, 103–112; (*c*) M. Chen, X. Wang, Z. Zhang, K. Sun, C. Cheng and F. Dang, *Mater. Des.*, 2016, **97**, 454–458.
11 J. Zhu, S. Wei, L. Zhang, Y. Mao, J. Ryu, P. Mavinakuli, A. B. Karki, D. P. Young and Z. Guo, *J. Phys. Chem. C*, 2010, **114**(39), 16335–16342.
12 C. Cheng, R. Fan, Y. Ren, T. Ding, L. Qian, J. Guo, X. Li, L. An, Y. Lei, Y. Yin and Z. Guo, *Nanoscale*, 2017, **9**(18), 5779–5787.
13 Y. Li and N. Engheta, *Phys. Rev. Appl.*, 2018, **10**(5), 054021.
14 C. Soukoulis, J. Zhou, T. Koschny, M. Kafesaki and E. Economou, *J. Phys.: Condens. Matter*, 2008, **20**(30), 304217.
15 D. Smith, W. Padilla, D. Vier, S. Nemat-Nasser and S. Schultz, *Phys. Rev. Lett.*, 2000, **84**(18), 4184.
16 C. Enkrich, M. Wegener, S. Linden, S. Burger, L. Zschiedrich, F. Schmidt, J. Zhou, Th. Koschny and C. Soukoulis, *Phys. Rev. Lett.*, 2005, **95**(20), 203901.
17 G. Dolling, C. Enkrich, M. Wegener, J. Zhou, C. Soukoulis and S. Linden, *Opt. Lett.*, 2005, **30**(23), 3198–3200.
18 G. Dolling, M. Wegener, C. Soukoulis and S. Linden, *Opt. Lett.*, 2007, **32**(1), 53–55.
19 P. Xie, Z. Wang, Z. Zhang, R. Fan, C. Cheng, H. Liu, Y. Liu, T. Li, C. Yan, N. Wang and Z. Guo, *J. Mater. Chem. C*, 2018, **6**, 5239–5249.
20 B. Li, G. Sui and W. Zhong, *Adv. Mater.*, 2009, **21**(41), 4176–4180.
21 C. Cheng, R. Fan, G. Fan, H. Liu, J. Zhang, J. Shen, Q. Ma, R. Wei and Z. Guo, *J. Mater. Chem. C*, 2019, **7**, 3160–3167.
22 G. Fan, Y. Zhao, J. Xin, Z. Zhang, P. Xie, C. Cheng, Y. Qu, Y. Liu, K. Sun and R. Fan, *J. Am. Ceram. Soc.*, 2020, **103**(1), 403–411.
23 P. Xie, Z. Wang, K. Sun, C. Cheng, Y. Liu and R. Fan, *Appl. Phys. Lett.*, 2017, **111**(11), 112903.
24 P. Xie, W. Sun, Y. Liu, A. Du, Z. Zhang, G. Wu and R. Fan, *Carbon*, 2018, **129**, 598–606.
25 P. Xie, Z. Zhang, K. Liu, L. Qian, F. Dang, Y. Liu, R. Fan, X. Wang and S. Dou, *Carbon*, 2017, **125**, 1–8.
26 A. Grigorenko, A. Geim, H. Gleeson, H. F. Gleeson, Y. Zhang, A. Firsov, I. Khrushchev and J. Petrovic, *Nature*, 2005, **438**, 335–338.
27 C. Nan, *Prog. Mater. Sci.*, 1993, **375**(1), 1–116.
28 C. Nan, Y. Shen and J. Ma, *Annu. Rev. Mater. Res.*, 2010, **40**, 131–151.
29 (*a*) B. Abeles, P. Sheng, M. Coutts and Y. Arie, *Adv. Phys.*, 1975, **24**(3), 407–461; (*b*) C. Grimaldi and I. Balberg, *Phys. Rev. Lett.*, 2006, **96**(6), 066602; (*c*) R. Hashemi and G. Weng, *Carbon*, 2016, **96**, 474–490.
30 (*a*) J. Chen, Q. Yu, X. Cui, M. Dong, J. Zhang, C. Wang, J. Fan, Y. Zhu and Z. Guo, *J. Mater. Chem. C*, 2019, **7**, 11710–11730; (*b*) H. Liu, Q. Li, Y. Bu, N. Zhang, C. Wang, C. Pan, L. Mi, Z. Guo, C. Liu and C. Shen, *Nano Energy*, 2019, **66**, 104143; (*c*) D. Jiang, Y. Wang, B. Li, C. Sun, Z. Wu, H. Yan, L. Xing, S. Qi, Y. Li, H. Liu, W. Xei, X. Wang, T. Ding and Z. Guo, *Macromol. Mater. Eng.*, 2019, **304**, 1900074; (*d*) H. Liu, Q. Li, S. Zhang, R. Yin, X. Liu, Y. He, K. Dai, C. Shan, J. Guo, C. Liu, C. Shen, X. Wang, N. Wang, Z. Wang, R. Wei and Z. Guo, *J. Mater. Chem. C*, 2018, **6**, 12121–12141; (*e*) S. Zhang, H. Liu, S. Yang, X. Shi, D. Zhang, C. Shan, L. Mi, C. Liu, C. Shen and Z. Guo, *ACS Appl. Mater. Interfaces*, 2019, **11**, 10922–10932.
31 (*a*) D. Jiang, V. Murugadoss, Y. Wang, J. Lin, T. Ding, Z. Wang, Q. Shao, C. Wang, H. Liu, N. Lu, R. Wei, S. Angaiah and Z. Guo, *Polym. Rev.*, 2019, **59**, 280–337; (*b*) C. Wang, V. Murugadoss, J. Kong, Z. He, X. Mai, Q. Shao, Y. Chen, L. Guo, C. Liu, S. Angaiah and Z. Guo, *Carbon*, 2018, **140**, 696–733; (*c*) N. Wu, D. Xu, Z. Wang, F. Wang, J. Liu, W. Liu, Q. Shao, H. Liu, Q. Gao and Z. Guo, *Carbon*, 2019, **145**, 433–444; (*d*) P. Xie, B. He, F. Dang, J. Lin, R. Fan, C. Hou, H. Liu, J. Zhang, Y. Ma and Z. Guo, *J. Mater. Chem. C*, 2018, **6**, 8812–8822; (*e*) L. Chen, J. Zhao, L. Wang, F. Peng, H. Liu, J. Zhang, J. Gu and Z. Guo, *Ceram. Int.*, 2019, **45**, 11756–11764.
32 Z. Rubin, S. Sunshine, M. Heaney, I. Bloom and I. Balberg, *Phys. Rev. B: Condens. Matter Mater. Phys.*, 1999, **59**(19), 12196.
33 I. Balberg, D. Azulay, J. Jedrzejewski and E. Savir, *Appl. Phys. Lett.*, 2014, **104**(25), 253109.
34 R. Mukherjee, Z. Huang and B. Nadgorny, *Appl. Phys. Lett.*, 2014, **105**(17), 173104.
35 S. Kale, F. Sabet, I. Jasiuk and M. Ostoja-Starzewski, *J. Appl. Phys.*, 2016, **120**(4), 045105.
36 P. Xie, K. Sun, Z. Wang, Y. Liu, R. Fan, Z. Zhang and G. Schumacher, *J. Alloys Compd.*, 2017, **725**, 1259–1263.
37 K. Yan, R. Fan, Z. Shi, L. Qian, Y. Wei, K. Sun and J. Li, *J. Mater. Chem. C*, 2014, **2**(6), 1028–1033.
38 C. Hou, Y. Oaki, E. Hosono, H. Lin, H. Imai, Y. Fan and F. Dang, *Mater. Des.*, 2016, **109**, 718–725.
39 C. Hou, Y. Hou, Y. Fan, Y. Zhai, Y. Wang, Z. Sun, R. Fan, F. Dang and J. Wang, *J. Mater. Chem. A*, 2018, **6**, 6967–6976.
40 (*a*) F. Dang, T. Hoshino, Y. Oaki, E. Hosono, H. Zhou and H. Imai, *Nanoscale*, 2013, **5**(6), 2352–2357; (*b*) H. Yin, D. Hu, X. Geng, H. Liu, Y. Wan, Z. Guo and P. Yang, *Mater. Lett.*, 2019, **255**, 126531; (*c*) Z. Zheng, H. Li, X. Zhang, H. Jiang, X. Geng, S. Li, H. Tu, X. Cheng, P. Yang and Y. Wan, *Nano Energy*, 2020, **68**, 104298.

41 (*a*) Y. Chen, P. Xu, H. Chen, Y. Li, W. Bu, Z. Shu, Y. Li, J. Zhang, L. Zhang, L. Pan, X. Cui, Z. Hua, J. Wang, L. Zhang and J. Shi, *Adv. Mater.*, 2013, **25**(22), 3100–3105; (*b*) H. Wei, H. Wang, A. Li, H. Li, D. Cui, M. Dong, J. Lin, J. Fan, J. Zhang, H. Hou, Y. Shi, D. Zhou and Z. Guo, *J. Alloys Compd.*, 2020, **820**, 153111.
42 J. Dyre and T. Schrøder, *Rev. Mod. Phys.*, 1999, **72**(3), 873–892.
43 A. Jonscher, *Nature*, 1977, **267**, 673–679.
44 X. Wang, Z. Shi, M. Chen, R. Fan, K. Yan, K. Sun, S. Pan and M. Yu, *J. Am. Ceram. Soc.*, 2014, **97**(10), 3223–3229.
45 I. Balberg, D. Azulay, D. Toker and O. Millo, *Int. J. Mod. Phys. B*, 2004, **18**(15), 2091–2121.
46 S. Fostner, R. Brown, J. Carr and S. Brown, *Phys. Rev. B: Condens. Matter Mater. Phys.*, 2014, **89**(7), 075402.
47 I. Balberg, *Carbon*, 2002, **40**(2), 139–143.
48 D. Azulay, I. Balberg, V. Chu, J. Conde and O. Millo, *Phys. Rev. B: Condens. Matter Mater. Phys.*, 2005, **71**(11), 113304.
49 D. Toker, D. Azulay, N. Shimoni, I. Balberg and O. Millo, *Phys. Rev. B: Condens. Matter Mater. Phys.*, 2003, **68**(4), 041403.
50 B. Abeles, H. Pinch and J. Gittleman, *Phys. Rev. Lett.*, 1975, **35**(4), 247.
51 P. Dirac, *The principles of quantum mechanics*, Oxford University Press, 1981.
52 J. Li, T. Li, Y. Zhou, W. Wu, L. Zhang and H. Li, *Phys. Chem. Chem. Phys.*, 2016, **18**(40), 28217–28226.
53 C. Wang and J. Callaway, *Phys. Rev. B: Solid State*, 1974, **9**(11), 4897.
54 N. Yousefi, X. Sun, X. Lin, X. Shen, J. Jia, B. Zhang, B. Tang, M. Chan and J. Kim, *Adv. Mater.*, 2014, **26**(31), 5480–5487.
55 Y. Jiang, X. Fu, Z. Zhang, W. Du, P. Xie, C. Cheng and R. Fan, *J. Alloys Compd.*, 2019, **804**, 305–313.
56 D. Turnbull and H. Ehrenreich, *Solid state physics*, Academic Press, 1991.
57 J. Pendry, A. Holden, W. Stewart and I. Youngs, *Phys. Rev. Lett.*, 1996, **76**(25), 4773.
58 J. Pendry, A. Holden, D. Robbins and W. Stewart, *J. Phys.: Condens. Matter*, 1998, **10**(22), 4785.
59 H. Shokrollahi and K. Janghorban, *J. Mater. Process. Technol.*, 2007, **189**(1), 1–12.
60 T. Liu, X. Xie, Y. Pang and S. Kobayashi, *J. Mater. Chem. C*, 2016, **4**(8), 1727–1735.
61 P. Xie, B. He, F. Dang, J. Lin, R. Fan, C. Hou, H. Liu, J. Zhang, Y. Ma and Z. Guo, *J. Mater. Chem. C*, 2018, **6**, 8812.
62 B. Zhao and C. Park, *J. Mater. Chem. C*, 2017, **5**, 6954–6961.
63 M. Han, X. Yin, H. Wu, Z. Hou, C. Song, X. Li, L. Zhang and L. Cheng, *ACS Appl. Mater. Interfaces*, 2016, **8**, 21011–21019.